PNAS
www.pnas.org

Supplementary Information for

Statistical reprogramming of macroscopic self-assembly with dynamic boundaries

Utku Culha[1], Zoey S. Davidson[1], Massimo Mastrangeli[2], and Metin Sitti[1,3]*

[1] Physical Intelligence Department, Max Planck Institute for Intelligent Systems, 70569 Stuttgart, Germany
[2] Electronic Components, Technology and Materials, Department of Microelectronics, Delft University of Technology, 2628CT Delft, The Netherlands
[3] School of Medicine and School of Engineering, Koç University, 34450 Istanbul, Turkey

*Corresponding author: Metin Sitti
*Email: sitti@is.mpg.de

This PDF file includes:

Supplementary text S1 to S9

Figures S1 to S9

Legends for Movies S1 to S5

SI References

Other supplementary materials for this manuscript include the following:

Movies S1 to S5

Supplementary Information Text

S1. Experimental Platform and Particle Tracking

Experimental platform. The confinement mechanism we used in our experiments is composed of six main components (Fig. S1a): (1) a bottom surface, (2) 12 identical moving leaves, (3) a rotating confinement wheel, (4) a DC motor, (5) four fixing gears and (6) a confining, transparent top lid. The bottom surface (20 cm x 20 cm x 0.5 cm, acrylic plate (Plexiglass® Evonik™)) was produced using a CO_2 laser cutter (Epilog Laser Mini). We referred to the center of the surface, where the particles slide during the experiments, as the *arena*. The perimeter of the arena contained the sliding rails and the holes that guide the linear motion of the leaves. We coated the arena with 3 µm-thick Parylene C to reduce frictional effects (heat production, contact electrification) with the sliding particles. Each leaf was 3 mm-thick, had a triangular shape and was fabricated out of the same acrylic material. There were two extrusions on each leaf structure: a column on the bottom, and a pushing pin on the top. The column fitted in the sliding rails of the bottom surface and the pin fitted in the circular slots on the confinement wheel. Both of these extrusions converted the rotational motion of the confinement wheel into the translational motion of the leaves and enforced them to slide on the surface. We coated the bottom surface of the leaves with 300 µm-thick copper film to minimize charge build-up upon contact electrification within the Parylene, and we electrically grounded the whole mechanism. The adjacent leaves were arranged in tight contact so that they preserved a dodecagonal arena shape at all positions. The confinement wheel fitted on top of the leaves and had gear teeth on its exterior side that meshed with another smaller gear fitted to the shaft of a DC motor (Maxon™ DCX®). This coupled gear mechanism made the sliding motion of the leaves bidirectional and reversible. We used Maxon's DC motor controller (Maxon™ EPOS4® 50/5 Module) to control the position and velocity of the confinement mechanism – that is, to control R and its linear rate of change over time $dR/dt = \dot{R}$. We could change R from R_{MAX} = 47.5 mm to R_{MIN} = 20.5 mm and $\dot{R}$ within the range of 0.042 mm/s to 46.240 mm/s. In our experiments, we used a subset of the total $\dot{R}$ range. Note that a linear radius rate of change corresponded to a *non*-linear rate of change in the arena volume. We additionally used four small gears to fix the confinement wheel to avoid shaking while the wheel rotated on its axis. There were two limit switches and a marker on the confinement wheel for calibration and homing procedures (Fig. S1b). A transparent lid fitted over the leaves and the central gap on the confinement wheel to confine the particles into the two-dimensional arena (see Movie S1). There was a 100 µm spacer in between the lid and the top of the leaves to avoid additional sliding friction with the particles. The complete mechanism was mounted on top of the aluminum platform of the orbital shaker The complete setup, except for the top-view high-speed camera, can be seen in Fig. S1b.

Particle tracking. A high-speed camera (Basler Ace acA800-510uc) was mounted on the same orbital shaker platform to sync the reference frame of the camera to that of the arena. This configuration allowed us to fix the arena in the reference frame of the camera and track the particle motion relative to the center of the arena. According to the camera's distance to the physical setup (~225 mm) and image resolution (800 x 600 pixel^2), we could achieve a resolution of ~0.195 mm per pixel. We used MATLAB®'s built-in image processing toolbox (1) to extract the high-contrast 'T'-shaped markers in a single grayscale image (Fig. S1d). We found the center of mass of the total number of pixels that corresponded to the T-marker and used this information to determine the position of a particle. We compared the performance of this method to a generic circular Hough transform (2) and found the difference between detected centroid points to be 0.19 ± 0.06 mm (*i.e.*, less than a pixel) for the average of 10^2 examples (Fig. S1d). We used the same toolbox to determine the orientation of each particle on the plane from the angle between the x-axis of the image and the long and short vertices of the T-shape. The high-speed image acquisition (360 frames per second) allowed us to easily associate two particles across consecutive frames by comparing their position and orientation data.

S2. Magnetic Model and Arena Coverage by Particles

In our experiments, the particles are confined within the 2D domain of the arena and interact with each other repulsively on the same horizontal plane, as sketched in Fig. S2a. Therefore we measured the magnetic repulsion force between a pair of approaching particles on a horizontal axis using a rheometer setup (TA Instruments, DHR-3). The measurements are compared with the theoretical dipole model in Fig. S2b. The modeled and measured forces agree very closely, hence we used the magnetic dipole model to approximate the magnetic force and magnetic potential energy between particles in the rest of our experiments using:

$$\vec{F}(\vec{r}, \overrightarrow{m_1}, \overrightarrow{m_2}) = \frac{3\mu_0}{4\pi|\vec{r}|^4}\left(\overrightarrow{m_2}(\overrightarrow{m_1}\cdot\hat{r}) + \overrightarrow{m_1}(\overrightarrow{m_2}\cdot\hat{r}) + \hat{r}(\overrightarrow{m_1}\cdot\overrightarrow{m_2}) - 5\hat{r}(\overrightarrow{m_1}\cdot\hat{r})(\overrightarrow{m_2}\cdot\hat{r})\right) \quad (1)$$

Equation (1) shows the magnetic force vector $\vec{F}$ that depends on the distance vector $\vec{r}$ and unit vector $\hat{r}$ that points between two magnetic dipoles with magnetic moments $\overrightarrow{m_1}$ and $\overrightarrow{m_2}$. In our experiments, each particle had the same magnetic moment $\overrightarrow{m_i} = [0 \quad 0 \quad B_r V/\mu_0]$ where B_r is the flux density (B_r = 1.32 T, 3 mm diameter, 1 mm height, N48 grade, Supermagnete, Fig. S1c), V is the volume of the cylindrical magnet ($V \cong 7.07 \times 10^{-9}$ m^3) and μ_0 is the permeability of the vacuum ($\mu_0 = 4\pi \times 10^{-7}$ H/m). As the particles were confined in a 2D domain in our experiments, we assumed $\vec{r} = [r_x \quad r_y \quad 0]$ and the unit vector $\hat{r}$ accordingly. Similarly, we approximated the magnetic potential energy $E_U = -\overrightarrow{m_i}\cdot\vec{B}(\vec{r})$, with the magnetic field $\vec{B}(\vec{r})$ measured at a distance $\vec{r}$ from for a single magnetic dipole with moment $\overrightarrow{m_i}$:

$$\vec{B}(\vec{r}) = \frac{\mu_0}{4\pi|\vec{r}|^3}3\left(\vec{r}/|\vec{r}|\right)\left(\left(\vec{r}/|\vec{r}|\right)\cdot\overrightarrow{m_i}\right) - \overrightarrow{m_i} \quad (2)$$

We calculated the total magnetic potential of the self-assembly patterns in our experiments by summing up the magnetic field shown in Equation (2) for all the 25 particles.

To show the importance of mutual inter-particle magnetic repulsion for a homogeneous exploration of the arena, we used a separate set of 25 particles (identical to the ones used in the experiments) and demagnetized their inner permanent magnets by heating them above their Curie temperature (~400°C). We placed these particles within the arena and recorded their position for 30 s while f_r = 6 Hz and $R = R_{MAX}$. Figure S2c shows the probability distribution function of their position as a 2D histogram that divides the dodecagonal arena into 100 x 100 equal-sized bins. It can be seen that the particles tend to follow the trajectory dominantly set by the orbital shaker (shown with the smaller dotted circle). Despite the disturbances caused by physical impacts with each other and the hard walls of the arena and the friction on the arena surface, the particles did not explore the arena homogeneously and got collected at the center while dissipating their energy (3). The influence of the magnetic repulsion can be easily appreciated when this result is compared with the case of magnetized particles and their arena exploration with f_r = 6 Hz, shown in Fig. S2g. In the latter case, the exploration was more homogenous thanks to the repulsion force between particles. These histogram figures also show the influence of f_r on particle exploration in addition to the magnetic repulsion. Even in the presence of magnetic repulsion, the particles remained mostly stationary if the shaking frequency was not high enough (*i.e.,* $f_r \leq 3$ Hz) to overcome static friction. Figure S2d shows the condition (f_r = 3.3 Hz) for which the particles could overcome the friction but their trajectories were governed by the magnetic repulsion and the orbital shaker motion. This trend started to diminish for f_r = 4 Hz and particles formed a cohesive structure noticeable as a circular path with $R \cong 30$ mm $\cong 6\rho$ in Fig. S2e. Increasing f_r from 5 Hz to 7 Hz, the particles gained more kinetic energy to work against the magnetic potential and hard interactions started to happen, and the particles consequently explored the available space more homogeneously. In all of the cases, particles tried to avoid close contact with each other to reduce the magnetic potential energy, hence they tended to escape the arena. However, the hard walls stopped them at the arena edges, as evidenced by a higher particle distribution probability at the hard boundaries (Fig. S2e-

h). Therefore, the homogeneous exploration of the particles excludes the dodecagonal strip that immediately neighbors the hard wall boundary.

S3. Physical Analogies with Brownian systems

To investigate the role of the shaking frequency (f_r) on the particle behavior, we performed 33 isochoric experiments with 25 magnetic particles under constant arena volume with radius $R = R_{MAX}$. We picked f_r values from the list [3.0, 3.3, 3.7, 4.0, 5.0, 5.3, 5.7, 6.0, 6.3, 6.7, 7.0] Hz and repeated three experiments for each value while video recording the motion of the particles for 30 s at the rate of 360 fps. We computed the radial distribution function $g(r)$ and performed mean-squared displacement analysis for all 10800 frames of each experiment.

We have previously observed that the static friction of the arena surface dominated the mobility of the particles when f_r = 3.0 Hz. The spiky $g(r)$ in Fig. S3a shows a clear sign of a mostly static structure that was preserved among the particles as they could not gain enough mobility and relocate even after 30 s of shaking. The maximum value of the mean-squared displacement (MSD) of these particles in Fig. S3c also shows that particles could not move more than ~ 5 mm in total. To this end, the static friction was the dominant force on the particles and the influence of the f_r could not be observed.

We started observing particle motion after $f_r \geq 3.3$ Hz. We saw that for f_r = 3.3 Hz, the particles gained certain mobility (max. MSD in Fig. S3c ≈ 14 mm) and the static structure between 25 particles started to disappear slowly (shown with a smoother g(r) in Fig. S3a). Even though particles were moving in this case, their trajectories (as shown in Fig. S2d) were still following the circular pattern governed by the orbital shaker and they could not explore the maximum area of the arena (the dashed horizontal line in Fig. S3c describes the maximum area a particle can cover within the assembly arena boundaries, $D_{max} = (2R_{MAX} - \rho)^2$. Only after $f_r \geq 4.0$ Hz, we could see that particles gained enough mobility to explore the assembly arena, but the magnetic potential field was still the dominant effect on the particle motion.

We further investigated the shaking frequency within the range where hard particle interactions became observable (as seen in Fig. S3b). In this range (*i.e.,* $f_r \geq 5.3$ Hz), the kinetic energy provided by the shaking balanced the active forces on the particles, revealing interesting interactions taking place in our system. Even though our particles are in the millimeter scale, the analysis of the particle MSDs (Fig. S3d) and of the probability distribution of velocities (Fig. S3e) and angular change of orientation (Fig. S3g) revealed behavior reminiscent of a Brownian system at certain time scales. For this analysis, we filtered out the orbital component from the particle motion due to the global mechanical forcing (4) (explained in detail in SI section S4). The particles experienced a sequence of ballistic and diffusive motion regimes between 0 − 0.05 s and 0.1 − 0.5 s respectively, before reaching saturation at around 3 s due to the hard boundaries of the arena (Fig. S3d). Particle velocities averaged over the x-coordinate (in the diffusive regime) are well fit by the 2D Maxwell-Boltzmann (*i.e.*, Rayleigh) distribution, $P(v) = (v/\sigma_f^2)\exp(-v^2/2\sigma_f^2)$, characterized by a single parameter, the velocity mode σ_f (Fig. S3e). Particle velocity increased with increasing f_r (Fig. S3c), and σ_f scaled linearly with f_r (Fig. S3f). The change in the orientation of the particles, $\Delta\Theta$, showed a behavior similar to a biased random walker. We calculated the distribution of $\Delta\Theta$ by finding the angular difference between each particle's orientation for every consecutive frame within the diffusive regime. As notable by the positive mean of the unfiltered distribution in Fig. S3g, the particles followed the orbital trajectory. The filtering of the global forcing yielded a zero-mean normal angular distribution, corresponding in the analogy to angular Brownian motion with memory. Accordingly, the updated particle orientation was selected within a finite range biased around the prior orientation (zero mean) and with equal likelihood toward positive or negative differences (symmetry).

The analysis indicates that the shaking frequency of the granular system at certain time scales was acting similarly to an effective temperature when $f_r \geq 5.3$ Hz. We aim to establish stronger correlations by increasing the particle count in our system in future works.

S4. Filtering of Shaking Frequencies

In our experiments, the particles moved on the arena surface propelled by the momentum transferred from the orbital shaker employing sliding friction and collisions with the hard arena walls. The shearing force applied by the shaker equally and synchronously to all particles scaled with their mass $m \cong 0.093$ g, $\ddot{x}(t) = -L\omega^2 \cos(\omega t)$ and $\ddot{y}(t) = -L\omega^2 \sin(\omega t)$ where $\omega = 2\pi f_r$. The orbital shaking generated a global forcing influence, such that the orbital motion component is equally superposed to the trajectory of all particles. However, the particle interactions depended on the mutual magnetic repulsion, collisions with each other, spatial particle densities and hard boundary effects. To extract and highlight the relative particle motion over the orbital forcing, we filtered out the influence of the orbital shaker (f_r) by applying a band-stop filter to the Fast Fourier Transform (FFT) on the x- and y-coordinates of the particles during the experiments (4). For a single experiment, we initially converted the particle coordinates into the frequency domain (Fig. S4a). It was found that the orbital shaking influenced the frequency space amplitudes up to three orders of magnitude near the shaking frequency, $f_r = 6$ Hz (see Fig. S4c for $f_r = 7$ Hz). We applied a band-stop filter centered at f_r with 2 Hz width to exclude the effects of the orbital motion and then inverse-FFTed the filtered signal. The band-stop filter collaterally removed the natural motion of the particles within the $f_r \pm 1$ Hz (e.g. [5 7] Hz in Fig. S4a) frequency range. However, as the components within the filtered spectrum had much lower amplitudes compared to the low-frequency components of the signal, the resulting motion of the particles was not significantly disturbed. We chose the width and amplitude of the filter within the range that did not influence the dynamics of the system based on our previous work on the kinetics of orbital shaking and the application of band-stop filtering (4).

The results of the FFT filtering can be seen in the mean squared displacement (MSD) data shown in Fig. S4b and 4d. Here we compare the average and the maximum MSD values of 25 particles during three experiments with and without the band-stop filter on x- and y-coordinates. The filtering excluded the cyclic motion of the particles without disturbing the interactions taking place in the overall particle system. The insets reveal that the particle motion was influenced by the global f_r. The maximum distance the particles can cover in longer periods was strictly constrained by the hard boundaries of our mechanism and is represented with the horizontal dashed line ($D_{max} = (2R_{MAX} - \rho)^2$). The particles were obviously constrained by this physical limit regardless of the applied filter; however, we noticed that the filtered particle trajectories tended to overcome this limit, as the FFT did not impose the hard boundaries. This excess amount did not impact the overall particle behavior and motion analysis.

S5. Particle Count

We chose $N = 25$ particles for our reprogrammable self-assembly experiments to guarantee stable states under full compression ($R = R_{MIN}$) while still maintaining the generalizability of our results. We defined structural stability as the topological permanence of the self-assembled patterns during shaking which can only be guaranteed when particles lose their mobility and cannot relocate within the compressed arena (see section S6 for the topological definition of self-assembled patterns). The underlying factors behind achieving stability with 25 particles were the geometrical limits of our confinement mechanism, the particle diameter (ρ), magnetic repulsion force and the range of the shaking frequency. The theoretical upper limit for the number of particles with $\rho = 5$ mm that can fit inside our assembly arena with $R = R_{MIN} = 20.5$ mm was 53. This number was calculated with a geometric optimization algorithm (5), so it did not consider magnetic repulsion between particles or any other mechanical forcing that might occur during confinement. Therefore, we expect the maximum number of magnetic particles fitting in our system to be lower than 53. Naturally, the maximum number of particles would increase with a larger confinement mechanism and/or smaller particle radius.

We investigated the minimum number of particles that guarantees the structural stability of the patterns in our system. We systematically increased the number of particles from 1 to 25 and

measured their kinetic and magnetic potential energies. For every experiment, we placed the chosen number of particles within the arena, agitated the system with shaking frequency f_r = 6 Hz and compressed the particles with the lowest rate ($\dot{R}$ = 0.079 mm/s) until we reached the minimum radius R_{MIN}. After the particles were compressed, we tracked their positions for 5 s and reported their energies. Figure S5a shows the calculated sum of kinetic and magnetic potential energy averages for the different number of particle experiments. It can be seen that the sum of the magnetic potential energy increased regularly and kinetic energy decreased with increasing N. We see a drastic drop in the kinetic energy after N = 21. Figure S5b shows the average kinetic energy for the sum of the particles and for each particle for different N. We see a slight increase in the energy sum until N = 3 as the number of particles increased, but after that point, the magnetic potential energy dominated the system and kinetic energy dropped. We also noticed a consistent drop in the average kinetic energy and velocity of single particles with increasing N (Fig S5b and Fig S5c). These results show that only after $N \geq 25$ the particles lost their mobility and allowed of meta-stable patterns during the maximum compression.

In our experiments, we had the option to choose $53 > N \geq 25$ to demonstrate the repeatable and reversible programming of self-assembled patterns. We performed 1200 experiments in total to show the statistical programmability of the 12 classes observed at $R = R_{MIN}$ – which do not necessarily cover all the possible configurations – for 25 particles. As the repeatability and reversibility of our system originated from the interactions between the particles and the dynamic hard boundaries, and not only from N, we chose N = 25 for the demonstration of our claims. We expect that more patterns with higher complexity can be observed with larger N (*i.e.,* $53 > N \geq 25$). Many more realizations of the programmable self-assembly process will be required to show the statistical programming in that case, along with larger computational effort for the tracking and analysis of particles. We expect that these foreseeable results, however, will not change the claims of our work, but rather only fortify them.

S6. Pattern Classification

In our work, we defined pattern classes based on the self-assembled patterns that emerge when the motion of the particles stopped (*i.e.* the compression is complete) for an arena volume given by $R = R_{MIN}$. In this state, the 25 magnetized particles are squeezed in a bounded area (η = 0.369), and their positions and orientations belong to a continuous space constrained by these boundaries. Within this space, each identical particle may assume a virtually infinite amount of position and orientation values, which makes a continuous pattern classification impossible. Therefore we preferred to identify the pattern classes based on the topological information which can be extracted from the relative position of the particles within the arena. For this purpose, we used the Delaunay triangulation method which takes the centroids of the particles on the 2D plane as the discrete vertices of triangles and generates a triangular network (*i.e.,* the topology) by interconnecting these vertices. Delaunay triangulation ensures that no centroid point remains inside the circumcircle of any triangle. The resulting triangulation is dual to the Voronoi tessellation wherein the vertices of the Voronoi diagram are the circumcenters of the triangles (6). In this work, we did not use the orientation information for classification as the particles were symmetric along planes normal to the surface of the arena.

We observed that the boundary of the arena played an important role in the formation of patterns during the confinement process. While its importance on the dynamics of self-assembly is the focus of our future work, its significance for pattern classification is explained here. We applied the Delaunay triangulation-based classification after the particles were fully compressed into a solid-like self-assembled structure. We represented the boundaries of the arena as virtual particles surrounding the actual magnetic particles. We found the centroid points of these virtual particles by dividing the boundary circle (radius $R = R_{MIN}$) into 500 equal points. We used MATLAB®'s built-in Delaunay triangulation method (1), which took as input the centroid position of 25 magnetized particles in addition to the 500 virtual boundary points and generated a triangular network (Fig. S6a).

Once the triangulation was generated, we identified the neighborhood connectivity between the particles starting from the boundary and sweeping towards the center of the arena. In the first step, we found the magnetic particles that had connecting edges to virtual boundary particles (the triangle edges are shown with blue lines connecting the particles in Fig. S6a). These particles made up the 'outer shell' in the pattern. We proceeded with the identification process by selecting the particles which had connections to the outer shell and named them as the 'middle shell'. The procedure ended by finding the remaining particles that had connections with the middle shell, which we named as the 'inner shell'. We denoted a pattern class based on the number of particles in each shell as $<\#_{outer}, \#_{middle}, \#_{inner}>$. Adopting the connectivity between particles instead of their absolute centroid position within the arena allowed us to classify different configurations into single classes (see Fig. S6a for examples of different configurations classified into the same class). Using this classification, we observed 12 distinct classes of patterns in our experiments after collecting 1200 pattern examples. The most frequently occurring class, i.e. Class 1 – <17, 7, 1> – was observed in 506 out of 1200 experiments, while Class 12 – <20, 5, 0> – occurred only once.

We observed at most three particle shells in our 25-particle experiments, hence we complemented the Delaunay triangulation method with a heuristic 3-shell template (circular shell structures have been previously identified and used in similar granular systems (7)). The template originated from Class 2 – <18, 6, 1>, which was the particle pattern with the lowest magnetic potential energy that we observed. The three shells had their origin at the center of the arena and had radii [0, 10.22, 18.09] mm. By applying this template to every pattern determined by the Delaunay triangulation, we could estimate the distance of the particles from their respective shells and detect jammed, metastable patterns. Figure S6b shows the heuristic template applied to a pattern detected with the Delaunay triangulation. The three red circles with straight lines represent the heuristic shells, and the circles with dashed lines are the middle points between each shell. As an example, the particle marked with 'x' in Fig S6b was originally depicted as an outer shell particle due to its connectivity with the boundary. However, by applying the heuristic template it appeared that this particle's centroid was closer to the middle shell (note that the particle fell inside the large circle with dashed lines) and therefore it should be depicted as a middle shell particle instead. The same logic was applied to the particle at the center. Via the heuristic template, the class was finally labeled as <17,7,1>. Other examples for the same heuristic template application can be seen in Fig. S6c.

The number of particles corrected with the heuristic in each Delaunay triangulation increased with $\dot{R}$ (the increased amount of corrections can be seen as the larger error bars in Fig 3a in the main text). In other words, for lower $\dot{R}$ the triangulation network and the heuristic pattern detected the same shell structures. This indicates that for lower $\dot{R}$ particles had a longer time to explore the space and relaxed into solid-like patterns that have higher circular symmetry and lower magnetic potential energy. Particles were instead trapped into more asymmetric, higher energy configurations for higher $\dot{R}$, which we could detect via the heuristic template. Fig. 3b shows the energetic signature of these detected patterns. While the overall energy of a single pattern class tended to increase with $\dot{R}$, the patterns detected and corrected via the heuristic had a higher average of magnetic potential energy compared to the patterns in the same class that didn't need correction (energy of the corrected patterns are shown with the shaded regions in Fig. 3b).

In addition to the detection of higher energy states, the heuristic also hinted towards the dynamic origin of the patterns. Figure S6c shows two other cases where classes have been corrected by the heuristic. On the top row, we see that Class 2 (<16,8,1>) was corrected into Class 4 (<16,7,2>) and on the bottom row, Class 9 (<19,6,0>) was corrected into Class 3 (<18,6,1>). Even though we were classifying the patterns in their fully compressed solid-like structure, the Delaunay triangulation gave important information about the history of the corrected particle. From the examples in the figure, we can guess from which shell and position the particle was traveling from before jamming due to the fast confinement rate. Our current work did not focus on the dynamic origins of self-assembled patterns; however, the combined use of Delaunay triangulation and heuristic template demonstrated potential for future improvements of reprogrammability and reversibility as shown in Fig.3c and d.

We additionally investigated the role of the number of virtual particles in the detection of pattern classes. Throughout our experiments, we used 500 virtual particles to represent the physical boundary. Figure S6d shows the number of misclassifications, ε, with the different number of boundary particles N, compared to N = 500 (represented with a star in the figure). The figure shows that when the least number of virtual particles were used (N = 30 was the maximum number of physical particles with ρ = 5 mm that can fit tightly around the boundary with $R = R_{MIN}$), there were only 12 patterns out of 1200 that were misclassified compared to when N = 500 (considering the Delaunay triangulation only). The difference dropped by increasing N and it reached zero when N = 200. As the heuristic was independent of N, the patterns were always classified in the same way.

S7. Reprogrammable Self-Assembled Classes

In our 1200 compression experiments, we observed 12 distinct classes classified with the combination of the Delaunay triangulation and the heuristic template methods at $R = R_{MIN}$. We established the correlation between the confinement rate $\dot{R}$ and the programmability $P(c)$ of each class. The majority of the patterns (95% of all the examples; *i.e.* 1130 out of 1200) were classified into Class 1 to 4 as shown in Fig. S7a. The remaining 70 patterns were classified into 8 distinct classes as shown in Fig. S7b. It can be seen that these classes occurred rarely and almost exclusively at faster $\dot{R}$. A closer inspection in Fig. 2c in the main text also reveals that these patterns generally emerged out of jammed particle configurations. These configurations were more likely to occur when compression took place in a short time and particles were not given the necessary time to relocate within the arena. Due to the same reason, the average magnetic potential energy of these remaining classes tended to be higher than the four most occurring classes, as seen in Fig. S7c. These classes also had low structural stability, meaning that their topology would change with the smallest perturbations in the arena radius (*e.g.,* ΔR).

Future work will investigate methods to increase the programmability of these jammed meta-stable patterns. We believe that reprogrammability of these patterns with higher selection probabilities may have interesting applications for materials science as their configurations may yield unique mechanical, optical or magnetic properties. In our current work, we have only investigated a feed-forward linear confinement method by changing the radius of the arena in a constant fashion. Changing the confinement profile into more complex, time and space asymmetric nonlinear methods may reveal different classes and increase the programmability of the currently observed patterns.

S8. Programmable Granular Stiffness

The magnetic repulsion among the particles in combination with our confinement mechanism allowed us to investigate the granular stiffness of the patterns (8). We initially investigated this stiffness by looking into the change of the total magnetic potential of a pattern while being compressed (Fig. S8a). Figure S8b (reproduced from Fig. 4b) shows ΔE_U versus ΔR for the top four classes. To get these data, we selected a pattern for each class with the $\dot{R}$ that yielded the highest $P(c)$ for that class (*i.e.,* $\dot{R}$ = 5.685 mm/s for Class 1, $\dot{R}$ = 0.079 mm/s for Class 2, $\dot{R}$ = 27.811 mm/s for Class 3 and $\dot{R}$ = 0.175 mm/s for Class 4). We compressed the shaking system with f_r = 6 Hz from $R = R_{MAX}$ until $R = R_{MIN} + \Delta d$. Within Δd, we allocated 2.6 mm for the total ΔR and maintained $R > R_{MIN}$ + 0.5 mm to avoid reading high motor torques close to maximum compression. After selecting a pattern at the given R, we stopped the shaking and advanced the compression across Δd with the lowest $\dot{R}$ = 0.079 mm/s. We recorded the particle positions for 33 s, which corresponded to 3 s for each of pre- and post-compression waiting times and 27 s for the confinement process. We used the particle positions and Equation (2) in Section S2 to find the progress of ΔE_U versus ΔR as shown in Fig. S8b. The different slopes reveal that the class topologies possessed different granular stiffness (specifically, Class 3 > Class 4 > Class 1 > Class 2).

When compressed into a solid-like state, the tensile particle structures exerted a force on the boundaries of the arena. We quantified this force using the current readings from the DC motor driving the confinement mechanism (*i.e.,* the leaves). While recording the particle positions during the compression as explained above, we also recorded the current output I_m and angular displacement θ_m of the motor using Maxon's DC controller unit (EPOS4® 50/5 Module). We calculated the work done by the motor as $W = (I_m \tau_m)\theta_m$ where τ_m = 22.915 mNm/A (motor torque constant). Figure S8c shows the work done by the motor with respect to ΔR based on this calculation. We observed a non-monotonic increase in work as the elastic magnetic structures are compressed. Similar to ΔE_U, different classes were associated with different slopes, confirming that our reprogrammable self-assembly method also selected for granular stiffness. The spring structures of the classes required motor work in the same descending class order with the ΔE_U. The spikes in the data are caused by changing current outputs due to the velocity profile control which drove the motor in constant confinement rate. We noticed that if the arena was compressed further (*i.e.,* from R_{MIN} + 0.5 mm to R_{MIN}), the leaves were enforced into higher mechanical locking, which caused higher magnitudes of motor torques. Therefore, we left a 0.5 mm space before the R_{MIN} to have more reliable motor current readings during the stiffness experiments.

S9. Programmable Magnetic Clutch

The magnetic properties of the particles also allowed us to investigate the reprogrammability of the continuous magnetic field over the self-assembled patterns in a 3D space. Similar to the granular stiffness experiments, we designed a mechanical system and transduced this programmable magnetic field into a mechanical clutch (*i.e.*, magnetic gear). As shown in Fig. S9a, we designed an auxiliary arm which housed the same type of permanent magnets that were embedded inside the particles. We designed three of these arms and placed the magnets at different distances $d \in$ [5, 10, 15] mm from the axis of rotation. We used the particle positions reported in Fig. 2c and replicated the self-assembled patterns by embedding 25 magnets inside an acrylic sheet, which we called the pattern disk. We placed this disk on a rheometer setup and fixed the auxiliary arm above the pattern such that the rotation axis of the arm was aligned with the center of the disk. We measured the torque applied from the 25 magnets inside the self-assembled pattern on to the magnet placed inside the rotating arm during three complete rotations. We measured these torque values from three different vertical heights $h \in$ [1, 3, 5] mm for each auxiliary arm with different magnet placements.

Figures S9 b-d show the average of these torque measurements for the patterns of Class 1, 2, 3, 4, 11 and 12. The magnetic profile read from each class was unique. This shows that the reprogrammable self-assembly of the magnetic patterns also selected three-dimensional magnetic field profiles, which could be transduced into reprogrammable magnetic clutching. These mechanisms may prove convenient for robotic applications where reconfigurable actuation stiffness/clutching is necessary (9).

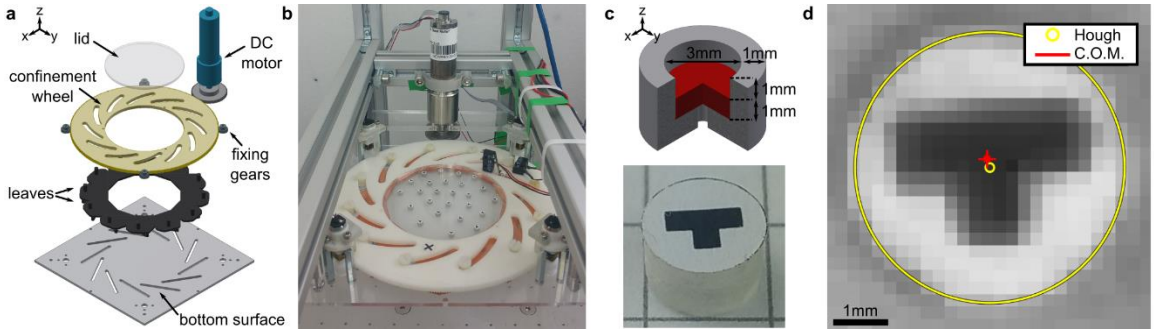

Fig. S1. **a.** CAD exploded view of the layered components making up the confinement mechanism (see also Movie S1). **b.** The experimental setup. There is a camera mounted over the confinement mechanism that is out of the frame of this image. **c.** Sliced CAD image (top) and photo of a single particle (bottom). A concentric cylindrical permanent magnet with a 3 mm diameter fits in the particle with its magnetic pole oriented along the particle's z-axis. **d.** Image of a single particle as captured by the top camera. Lines compare two centroid finding methods: center of mass (C.O.M.) vs. circular Hough transform.

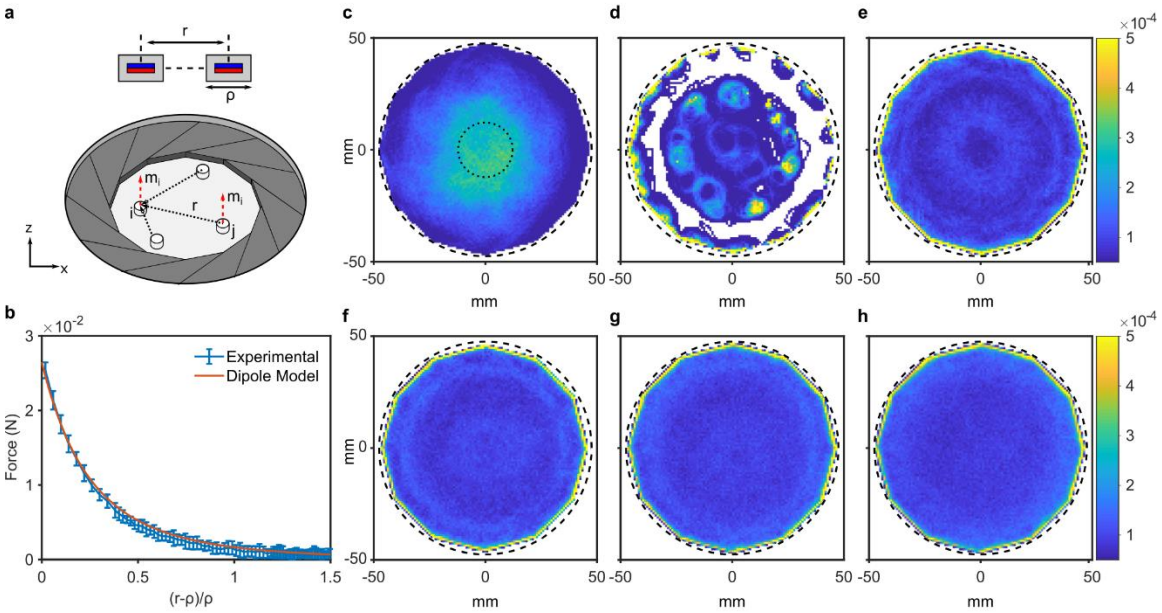

Fig. S2. a. Planar configuration of the particles embedded with permanent magnets. The distance r measures the horizontal distance between the centers of two particles (diameter ρ = 5 mm). Each particle's inner permanent magnet (of 3 mm diameter) has a magnetic moment m_i normal to the arena surface. **b.** The repulsive force between two identical magnets measured experimentally vs. the magnetic dipole model. **c.** Arena coverage of demagnetized particles, *i.e.* the probability distribution of the position of 25 particles within the confined assembly area with $R = R_{MAX}$ (shown with the dashed circle), with demagnetized permanent magnets while f_r = 6 Hz. The inner dotted circle represents the orbit of the shaker with radius L = 12.6 mm. **d-h**. Arena coverage of magnetized particles for different shaking frequencies: f_r = 3.3 Hz (**d**), f_r = 4 Hz (**e**), f_r = 5 Hz (**f**), f_r = 6 Hz (**g**) and f_r = 7 Hz (**h**).

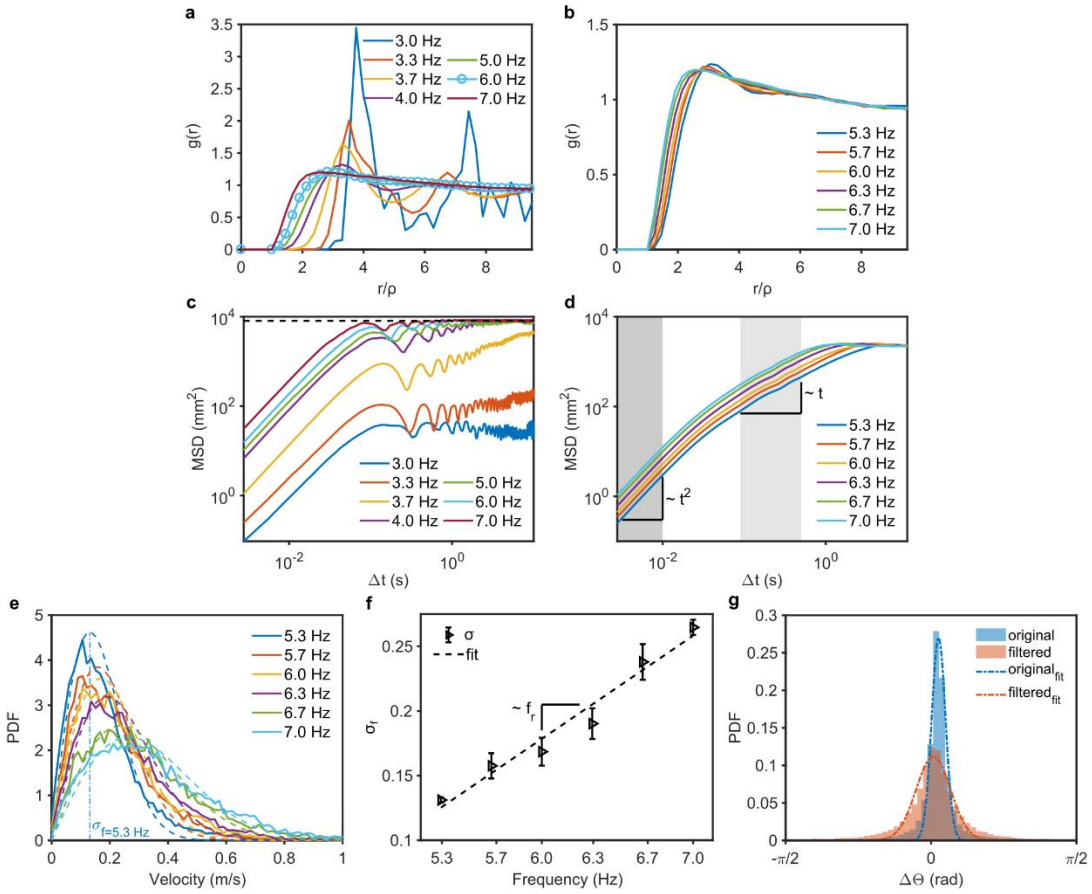

Fig. S3. a. Radial distribution function $g(r)$ for 25 particles inside the arena with $R = R_{MAX}$ for different shaking frequencies f_r from 3 Hz to 7 Hz. **b.** Focus on the $g(r)$ function within the range 7 Hz ≥ f_r ≥ 5.3 Hz where hard interactions are dominant. **c.** Maximum values of the mean-squared displacement analysis based on the unfiltered particle trajectories (average over 3 experiments per frequency value). The horizontal dashed line shows the hard boundary limit. Results are shown on a double logarithmic scale. **d.** Mean-squared displacement analysis within the 7 Hz ≥ f_r ≥ 5.3 Hz range. Marked regions represent the ballistic (~t^2) and diffusive (~t) regimes of motion, respectively. **e.** Average velocity distribution of the particles within the diffusive regime (~0.1 to ~0.5s). Dashed lines show the Rayleigh distributions fitted over the experimental data. **f.** The linear relation between velocity mode σ_f versus f_r. **g.** The probability distribution of angular change of particle orientation from the previous step ($\Delta\Theta$) within the diffusive regime (~0.1 to ~0.5s) for f_r = 6 Hz. Dashed lines show the normal distributions fitted over the experimental data. Note that this corresponds also to a Gaussian distribution of angular velocities since the angular orientation difference was sampled across adjacent image frames at a constant frame rate (360 fps).

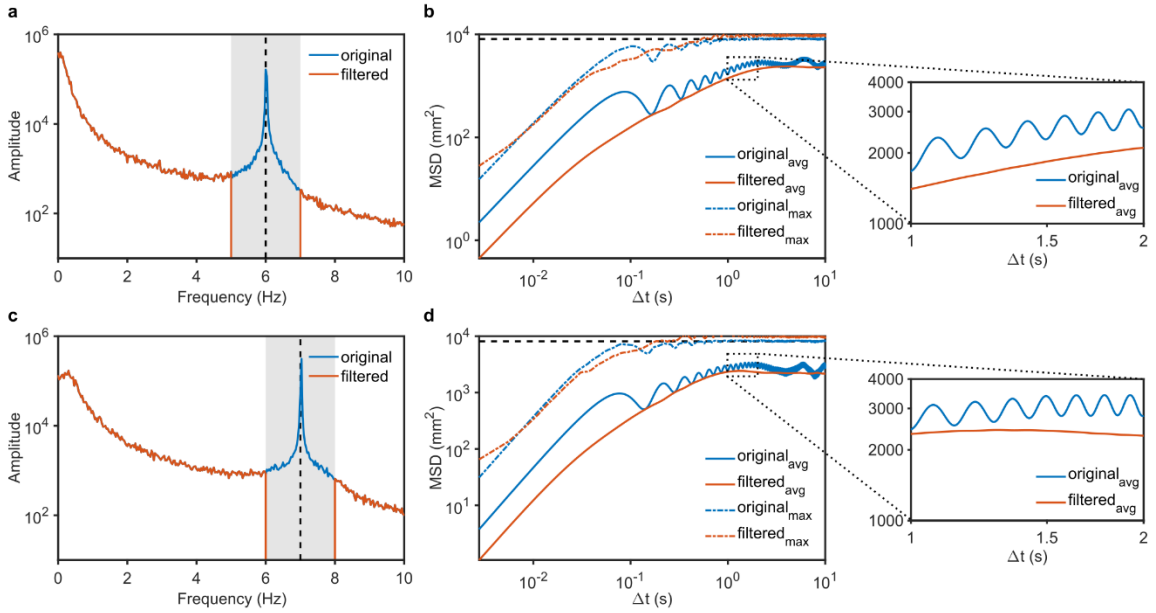

Fig. S4. a. The spectrum of the x-coordinate of 25 particles during a 30s isochoric experiment with f_r = 6 Hz shown on a semi-logarithmic plot. A band-stop filter with a 2 Hz width is applied to exclude the influence of the global mechanical forcing by the orbital shaker. **b.** Average and maximum MSD values before and after the filtering for the same experiment shown on a logarithmic scale. The inset figure shows the average MSDs within 1 s interval to emphasize the influence of f_r. **c.** The spectrum of the x-coordinate of 25 particles during a 30s isochoric experiment with f_r = 7 Hz shown on a y-semi-logarithmic plot. **d.** Average and maximum MSD values before and after the filtering for the same experiment shown on a logarithmic scale. The inset figure shows the average MSDs within 1 s interval to emphasize the influence of f_r.

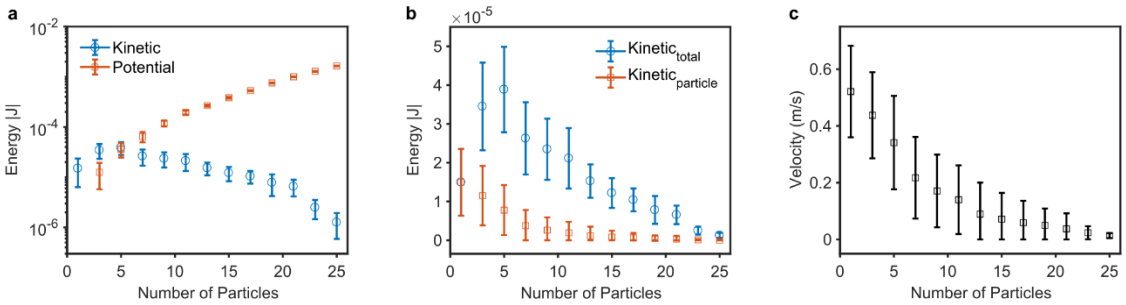

Fig. S5. **a.** Total average magnetic and kinetic energies of the different number of particles. **b.** The average of the sum of kinetic energies compared with the average kinetic energy of a single particle for the different number of particles. **c.** The average velocity for the different number of particles. All plots show the averages calculated from experiments when the system is fully compressed ($R = R_{MIN}$) and shaken for 5 seconds with f_r = 6 Hz.

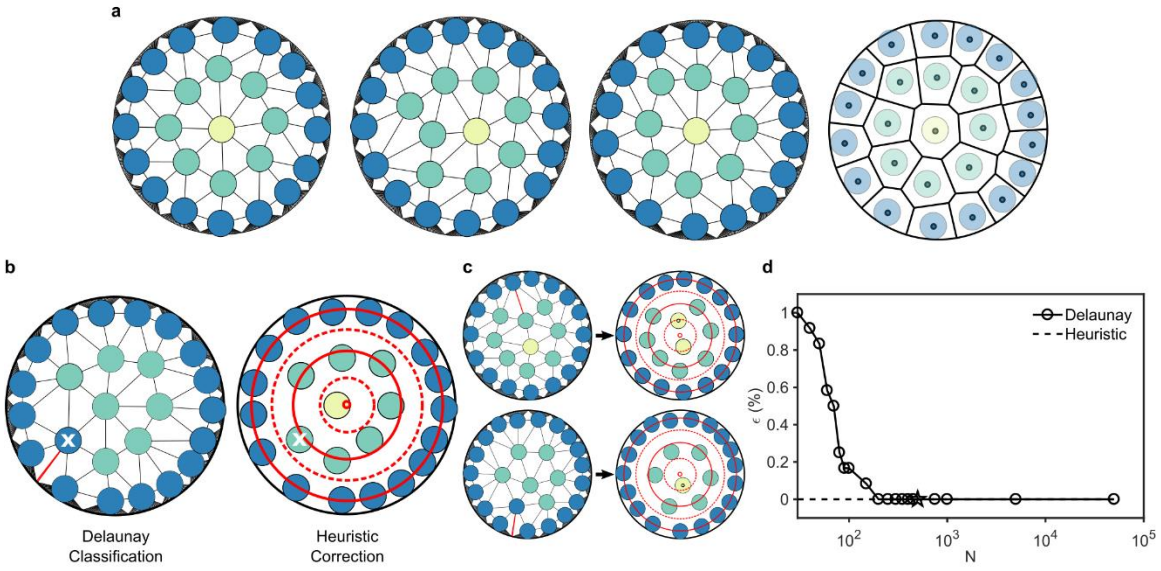

Fig. S6. a. Delaunay triangulation-based classification for a class out of sample patterns. Full circles represent magnetic particles (vertices) and lines represent the connecting edges. Different colors represent the shells of the structure (*i.e.,* blue-outer, green-middle, yellow-inner). Blue colored particles are connected to 500 virtual particles that represent the physical boundary. The first thee patterns belong to particle configurations from different experiments, yet they are classified into the same class (Class 2) with Delaunay triangulation. Third and fourth patterns are the same; the third pattern is shown with Delaunay triangulation, the fourth pattern is its Voronoi duality. **b.** Example case for a mismatch pattern. The particle marked with 'x' is counted as a part of the outer ring due to an edge connection with the boundary in the triangulation method and is classified as <18,7,0>. Correction of the previous topology with the heuristic template shown with red (straight and dotted) circles. The marked particle is now a part of the middle ring. The particle at the center is consequently identified and the pattern is corrected as <17,7,1>. **c.** Examples of heuristic correction of classes that hint at the dynamic origin and meta-stable nature of some patterns. Class 2 corrected to Class 4 (top) and Class 9 corrected to Class 3 (bottom). **d.** Error ratio ϵ vs. the number of virtual particles on the boundary (N) during the classification process. Corrections via the heuristic always eliminate the errors independent of N.

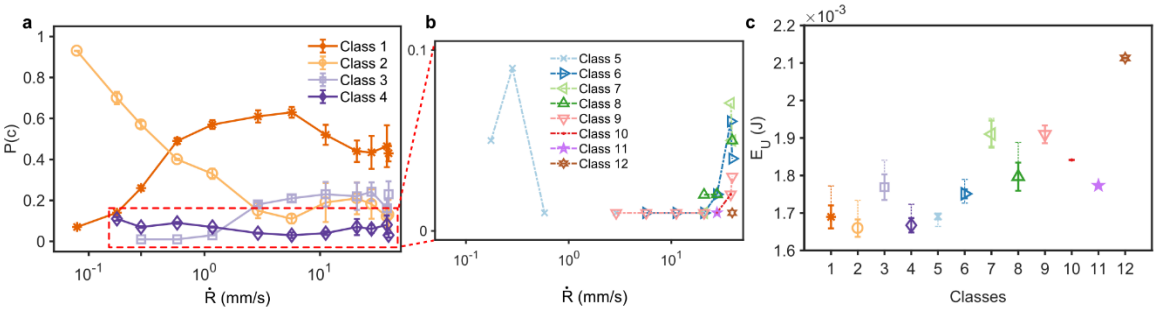

Fig. S7. **a.** Statistical programmability of the top four most occurring classes within 1200 compression experiments (reproduced from Fig. 3a). **b.** Statistical programmability of the remaining 8 classes, which occur for the fast range of $\dot{R}$ with low probability (*i.e.* P(c) < 0.1). **c.** The average magnetic potential energies of the classes calculated from all the patterns observed across the complete $\dot{R}$ range. The dashed lines represent the magnetic potential energies of the mismatch patterns belonging to the corresponding class. The classes are color and marker coded consistently across the figures.

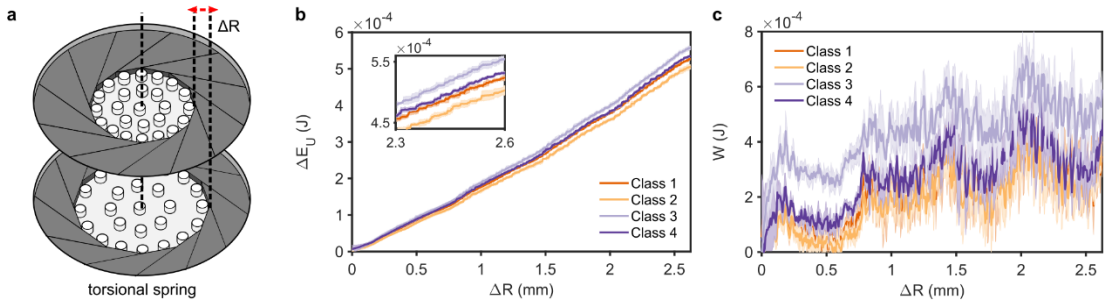

Fig. S8. a. Sketch of the two-dimensional stiffness experiment. ΔR corresponds to the perturbation of the arena radius. **b.** Change in the magnetic potential energy *vs* perturbation of arena radius **c.** The work done by the DC motor during the stiffness experiments.

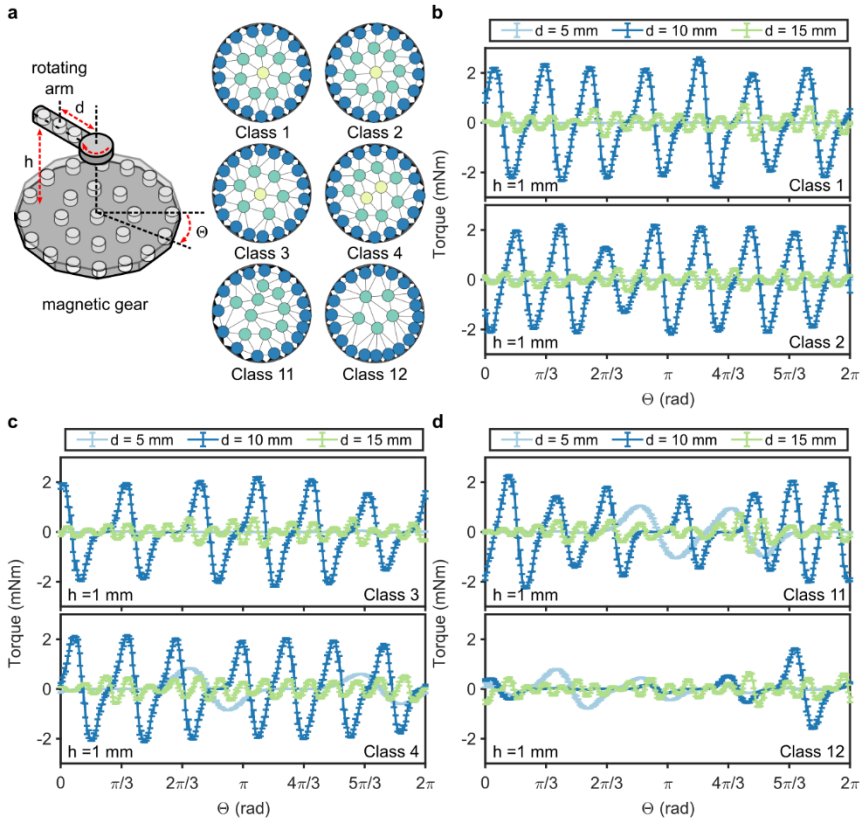

Fig. S9. a. Sketch of the reprogrammable magnetic clutch/gear experiments. *h* is the vertical distance of the rotating arm from the pattern disk, *d* is the distance of each magnet inside the arm to the rotation axis, and *Θ* is the rotation of the arm calculated positive in the clockwise direction from the x-axis of the pattern. The 6 pattern classes used in these experiments are shown for reference. **b.** Average torque profiles measured by the rheometer from the rotating arm at *h* = 1 mm for Class 1 and 2. **c.** Torque profiles for Class 3 and 4. **d.** Torque profiles for Class 11 and 12. Torque measurements in **b-d** are the average of three complete rotations.

Movie S1. CAD animation of the confinement mechanism.

Movie S2. Athermal (*i.e.* $f_r = 0$ Hz) compression sequence. Three sample cases of pattern classes showing the dependence on initial particle configuration in the absence of orbital shaking. Confinement rate for both compression and decompression is $|\dot{R}| = 20.81$ mm/s.

Movie S3. Programming (selecting) pattern Class 1 <17,7,1>. Confinement rate for compression is $\dot{R} = 5.69$ mm/s. Playback at 1x.

Movie S4. Programming (selecting) pattern Class 2 <16,8,1>. Confinement rate for compression is $\dot{R} = 0.18$ mm/s. Playback at 5x.

Movie S5. Reprogramming pattern classes with different confinement rates. Programming pattern Class 2 with $\dot{R} = 0.18$ mm/s (playback at 10x). Reversing the system by decompressing with $\dot{R} = -20.81$ mm/s (playback at 0.5x). Programming pattern Class 1 with $\dot{R} = 5.69$ mm/s (playback at 2x).

References

1. MATLAB 2017a and Image Processing Toolbox 10.0 (The Mathworks, Inc., Natick, Massachusetts, United States.
2. Davies ER (2004) *Machine Vision: Theory, Algorithms, Practicalities* (Elsevier).
3. Scherer MA, Kötter K, Markus M, Goles E, & Rehberg I (2000) Swirling granular solidlike clusters. *Phys. Rev. E* 61(4):4069.
4. Ipparthi D*, et al.* (2018) Kinetics of orbitally shaken particles constrained to two dimensions. *Phys. Rev. E* 98(4):042137.
5. Graham RL, Lubachevsky BD, Nurmela KJ, & Östergård PR (1998) Dense packings of congruent circles in a circle. *Discrete Mathematics* 181(1-3):139-154.
6. Okabe A, Boots B, Sugihara K, & Chiu SN (2009) *Spatial Tessellations: Concepts and Applications of Voronoi Diagrams* (John Wiley & Sons).
7. Kötter K, Goles E, & Markus M (1999) Shell structures with “magic numbers” of spheres in a swirled dish. *Phys. Rev. E* 60(6):7182.
8. Hemmerle A, Schröter M, & Goehring L (2016) A cohesive granular material with tunable elasticity. *Sci. Rep.* 6:35650.
9. Woodward MA & Sitti M (2019) Tailored Magnetic Springs for Shape-Memory Alloy Actuated Mechanisms in Miniature Robots. *IEEE Transactions on Robotics*.